

3-D characteristics of conical vortex around large-span flat roof by PIV technique

Huyue Sun^a and Jihong Ye^{*}

Key Laboratory of Concrete and Pre-stressed Concrete Structures of China Ministry of Education,
Southeast University, Nanjing 210018, China

(Received May 15, 2015, Revised April 11, 2016, Accepted April 19, 2016)

Abstract. Conical vortices generated at the corner regions of large-span flat roofs have been investigated by using the Particle Image Velocimetry (PIV) technique. Mean and instantaneous vector fields for velocity, vorticity, and streamlines were measured at three visual planes and for two different flow angles of 15°. The results indicated that conical vortices occur when the wind is not perpendicular to the front edge. The location of the leading edge corresponding to the negative peak vorticity and maximum turbulent kinetic energy was found at the center of the conical vortex. The wind pressure reaches the maximum near the leading edge roof corner, and a triangle of severe suction zone appears downstream. The mean pressure in uniform flow is greater than that under turbulent flow condition, while a significant increase in the fluctuating wind pressure occurs in turbulent streams. From its emergence to stability, the shape of the vortex cross-section is nearly elliptical, with increasing area. The angle that forms between the vortex axis and the leading edge is much smaller in turbulent streams. The detailed flow structures and characteristics obtained through FLUENT simulation are in agreement with the experimental results. The three dimensional (3-D) structure of the conical vortices is clearly observed from the comprehensive arrangement of several visual planes, and the inner link was established between the vortex evolution process, vortex core position and pressure distribution.

Keywords: flat roof; conical vortices; PIV; flow structure; FLUENT simulation

1. Introduction

Wind is one of the most destructive disasters in nature; previous wind disaster surveys indicate that most destroyed buildings are large-span roofs and low-rise buildings. Due to their intrinsic configuration, large-span roofs are always located at the bottom of the atmospheric boundary layer, which experiences rapid changes in speed and high turbulence intensity. When wind approaches a building at a certain angle, it will undergo complex flow separation, along with blocked air flow over the roof or around the sides. The flow cannot negotiate the sharp eaves completely because of the viscosity of the air. As a result, the wind separates at the windward apex of the roof and forms a pair of vortices, called conical vortices, at both sides. The worst suction induced by conical vortices is generated at the leading edge and the windward corners on the roof, which finally

^{*}Corresponding author, Professor, E-mail: yjihong@seu.edu.cn

^a Ph.D., E-mail: sunhuyue@163.com

causes catastrophic structural destruction. Therefore, the study of the characteristics of conical vortices, along with their formation mechanisms and evolution laws, is one of the key researches areas in the current field of wind engineering.

A flow visualization experiment is the most direct and effective method for studying the morphological characteristics of conical vortices. The three typical methods for visual experiments are following tufts, the trace technique and the PIV technique. Vector fields for velocity and vorticity cannot be measured using the first two approaches, as only the vortex structure can be obtained. However, PIV is a non-invasive whole-field velocimetry technique, which can yield the instantaneous velocity field and the vorticity field.

In this paper, we focus on flat roof structures, as many works on a flow visualization experiment of the conical vortices have been considered by many domestic and overseas scholars. Full-scale experiments were conducted on the low-rise experimental building by Wu at Texas Tech University (TTU) (Wu *et al.* 2001). The results showed that the formation of conical vortices is related to both horizontal and vertical wind angles of attack. Bank *et al.* (2000) also performed a flow visualization study of conical vortices behavior in the wind tunnels. He noted that the greatest suction was found to follow directly beneath the moving vortex core. For uniform flow field, the magnitude of the suction beneath the core is inversely proportional to the vortex size; however, the side with the conical vortex interchanges randomly in short time intervals for turbulent flow. This phenomenon is called vortex intermittency. Kim *et al.* (2001) revealed that a pair of counter rotating conical vortices, secondary vortices, and tertiary vortices was found clearly by using the PIV technique and also determined the vortex velocity and vorticity field in different wind directions. Zhao (1997) clarified the shape change of vortices under the different attack angles on the roof of a low-rise building through the flow visualization technique. The wind loading on the roof of a large hangar was investigated using a wind tunnel simulation (Gu *et al.* 2008). The results indicated that under certain wind directions, a conical vortex or a pair of conical vortex appears above the roof. The strong peak local negative pressure induced by the conical vortex is the main reason for the destruction on the roof, but quantitative parameters of vortices could not be obtained from the test. Li (2007) compared the surface pressures for the full-scale and model-scale TTU building using the conventional measurements and the flow visualization technique. Instantaneous flow trace figures of the vortices were obtained. However, the distribution of the velocity vector of the conical vortex was not provided, and no further study regarding the peak suction induced by conical vortices was presented. Flow visualization of conical vortices on large-span flat and saddle roofs was performed in a wind tunnel (Ye and Dong 2014). The streamline and vorticity field of visual planes on large-span roofs were given by PIV, and they confirmed the influence of wind direction and roof curvature on the appearance of conical vortices.

In summary, most studies involving flow visualization experiments of conical vortex behavior concentrated on qualitative assessments. Although the existence of a vortex can be confirmed, the results do not provide the quantitative velocity fields; in addition, the time-average conical vortex structure was obtained only for single-flow cases in the initial research. Therefore, in this study, flow visualization, which was conducted in a wind tunnel using PIV, of the conical vortex phenomenon on a 3-D flat roof was observed for multiple arrangements of visual planes. In addition to determining the average streamlines and vorticity field, the instantaneous trail regarding the vortex movements and velocity distributions above the roof surface at the visual planes are also measured in uniform and turbulent streams, simultaneously; the numerical simulation method was used to reproduce the 3-D characteristics of the conical vortices and the wind pressure distribution in two flow fields.

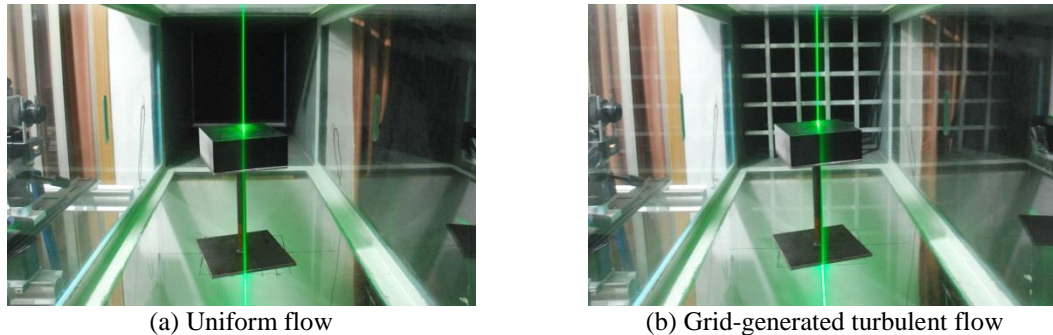


Fig. 1 Two types of wind field experiments

2. PIV experimental facilities and methods

2.1 Experimental setup

A flow visualization study of conical vortex behavior was performed in the TJ-4 atmospheric boundary layer wind tunnel at the Wind Engineering Research Center of Tongji University, Shanghai, China. The working region is 5 m long and contains a removable segment, a middle segment, and a terminal fixed segment. The model was placed in the middle section, which has a test section of dimensions of 0.8 m × 0.8 m × 2.0 m with glass palettes at all the sides, and the maximum sustained free stream velocity can reach up to 30 m/s.

Given the size of the laser section (0.5 m × 0.2 m) in the PIV experiment, the model has a dimension of 0.21 m × 0.21 m × 0.084 m (L×W×H). To obtain a rigid body and minimize the reflection of the laser sheet beam, the model was manufactured using black Plexiglas. There is a transparent glass box around the test section, and the vertical sheet aligned with the flow direction is illuminated by the laser beam passing through a cylindrical lens located above the test section. A CMOS camera was placed perpendicular to the laser beam, and the camera lens was set at a height equal to the center of the glass panels, approximately 1.5 m above the ground.

The free stream velocity was fixed to be 10 m/s, and the turbulent boundary layer approaching the model in a wind tunnel was characterized by a uniform and equal grid-generated turbulent flow field, as shown in Fig. 1. No blockage was placed ahead of the model in uniform flow; regarding the turbulent boundary layer, the grille bar width is 0.025 m, with a spacing of 0.14 m, and the porosity is 72%. The cube model was located 1.1 m downstream from the grid section entrance in the middle fixed segment. The flow field was calibrated by a 3-D wind speed measuring instrument, ensuring that the longitudinal turbulence intensity at the top of the model was approximately 10%.

2.2 Test program

The PIV system used in the study consisted of a Nd: YAG double-cavity laser with a pulse energy of 200 mJ at a wavelength 532 nm, a high-speed CMOS camera, a high-speed controller, an aerosol generator and a personal computer. To record the flow around the model, the camera operates at a frequency of 200 Hz, and the time interval between two successive images is 5 ms.

The size of the interrogation window was selected as $2.4\text{K} \times 1.8\text{K}$, and the frame rate is 480 fps for the full resolution. The PIV processor is connected to the computer and is controlled by the data acquisition program. The velocity fields were obtained and recorded on a computer, while the Davis 8.0 program controlled the acquisition process.

For the tracer particles, DEHS seeding fluid was used. This oily substance is known to satisfy the general specification of PIV seeding particles. For generation of the tracer particles, four atomizer nozzles were used to pressurize the seeding particles into the wind tunnel through nitrogen via a pressure controller when the oil was widely distributed. This method does not interfere with the flow field in the wind tunnel, thus ensuring the accuracy of the PIV measurement.

To investigate the 3-D flow structures around the model, three visual planes with a relatively larger area were captured at both sides of the roof diagonal. The planes were set to be parallel to the flow direction and located 67 mm, 67 mm and 134 mm from the windward vortex, as shown in Fig. 2, which are referred to as plane 1, plane 2 and plane 3, respectively, in this paper.

3. Results and discussion

3.1 Conical vortices in uniform flow (time-averaged characteristics)

The streamlines in the visual plane 1 of the conical vortex at a wind direction of 15° are shown in Fig. 3(a), which indicated that no eddy adhered to the roof, and that the streamlines were only bent slightly. The approaching flow direction was close to being parallel to the secondary windward side, with a wind angle of 15° , and no flow wash-up over this roof edge was found; hence, no recognizable conical vortices are present at visual plane 1. Figs. 3(b) and 3(c) show both the vorticity and velocity distributions of the averaged flow fields at the visual plane 1 of the conical vortices. A rapid flow appeared on the roof because no vortex formed and no reversal flow was present. The velocity of the flow decreased as it headed downstream due to viscous force. Generally, a high velocity gradient with a high strain rate and vorticity was observed. The velocity gradients that close to the roof surface reached a maximum as a direct result of the large absolute value of the vorticity. A smaller positive vorticity is distributed uniformly on the top of the plane, indicating no obvious effect from the vortices.

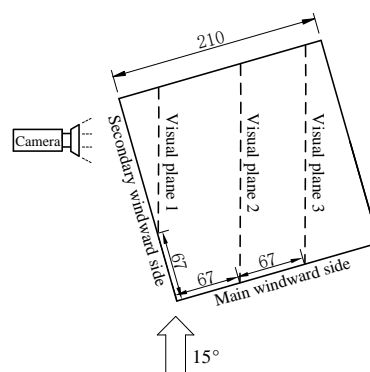


Fig. 2 Visual plane position (unit: mm)

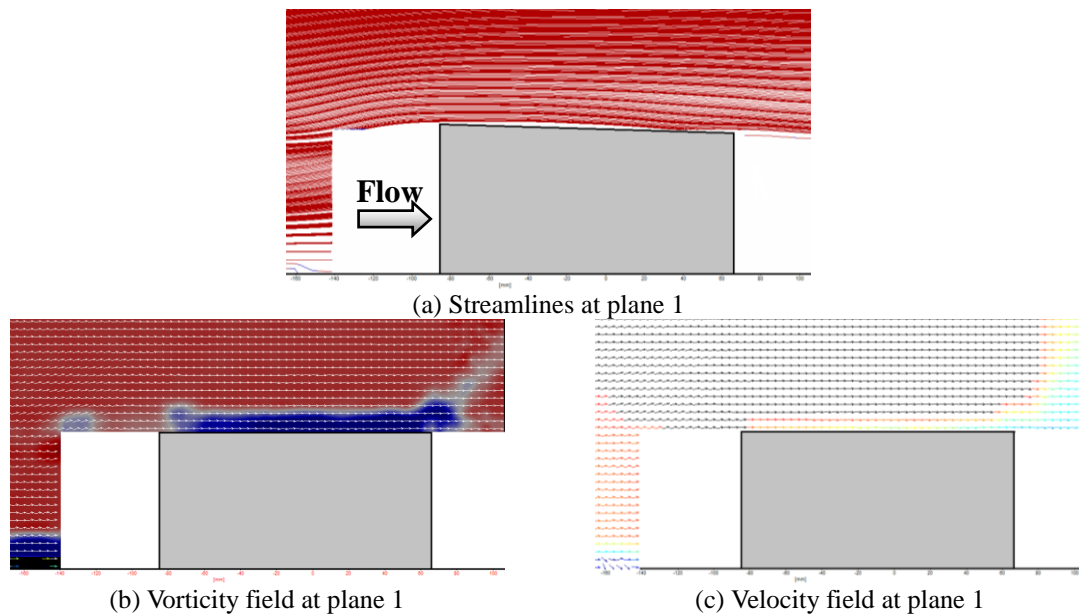


Fig. 3 Streamlines, vorticity and velocity fields of the conical vortices (uniform flow)

The streamline and vorticity distributions by an ensemble averaging taken at visual plane 2 and plane 3 for the case of a 15° wind direction are shown in Fig. 4. From a morphological perspective, the vortex sections formed near the elliptical shape and were found to cling to the roof along the windward edge on upwind face. The mean height of the vortex core was quite large. The negative vorticity was distributed over the conical vortex, indicating that flow reversal was dominant; however, the absolute value of vorticity between the vortex core and the roof was much smaller, which indicates that the vortex effect of this area became weaker. The region below the conical vortex exhibited flow reversal, which demonstrated that the fluid rotation and the incident flow were in opposite directions, thereby providing favorable conditions for the conical vortex formation. The magnitude of vorticity near the edge of the roof was larger, which manifested itself in the fluid rotating slightly faster. A dramatic velocity change along height direction was observed, and the velocity gradient of flow field was great found to be high, which also confirmed the existence of the eddy. Greater suction was induced under negative vorticity on the roof surface, and positive vorticity was observed in the upper portion far away from the roof surface. Comparing visual plane 2 and plane 3, the vortex core heights are found to be nearly equal, whereas the cross-sectional area in plane 3 is significantly greater than that in plane 2. Furthermore, the distance of the vortex core from the windward edge is also greater for plane 3 compared to plane 2 because the vortex axis movement is around the conical vortex trajectory in a side-to-side motion and the vortex axis at a fixed angle to the leading edge.

Figs. 5 and 6 show the vertical distribution of the horizontal mean velocity contained in the recirculation zone on the roof and the location of the vortex core point for plane 2 and plane 3 in uniform flow. As shown in Fig. 5(a), the roof surface is divided into ten equal sections which are named section 0 to section 10 in turn. For example, in section 0, the velocity of all points at the start is 0 m/s, while at the end; the velocity is 10 m/s. The velocities of other points in the middle are illustrated by the distance of each point from the start by a linear interpolation. These rules apply in all the other sections.

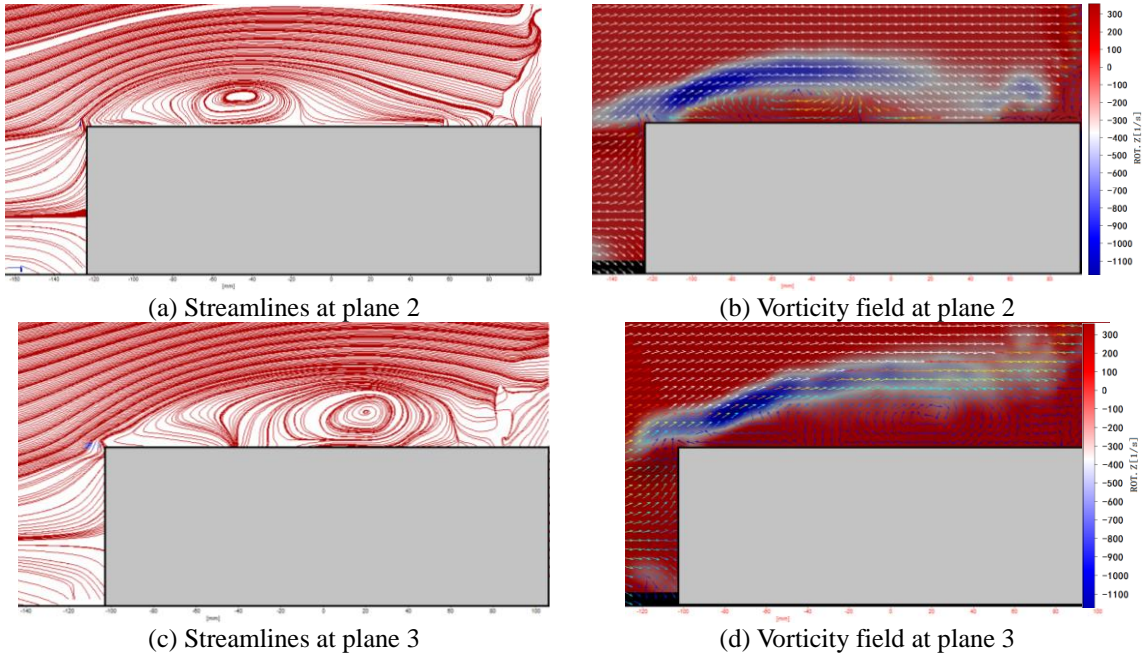


Fig. 4 Streamlines and vorticity field of plane 2 and plane 3 (uniform flow)

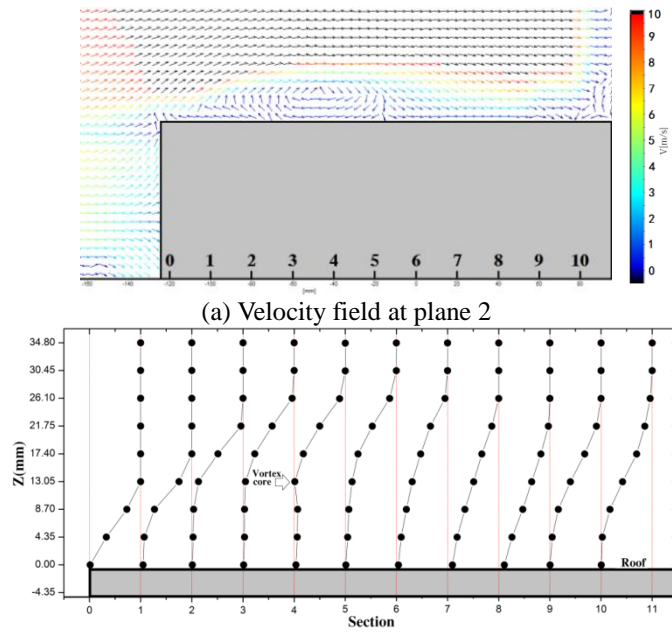


Fig. 5 The distribution of the along-wind direction velocity (uniform flow)

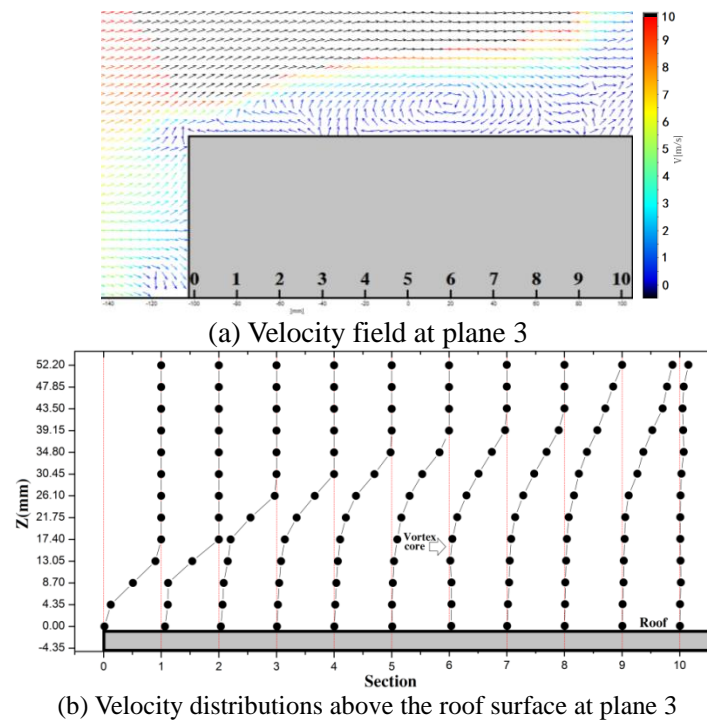


Fig. 6 The distribution of the along-wind direction velocity (uniform flow)

According to Figs. 5 and 6, the velocity at the boundary layer is much lower. In addition, at the starting edge of section 0, when the separated shear layer meets the reverse flow, the velocity gradient is increased. For section 4 of visual plane 2, the first inflection point lies between the roof surface and the vortex core, when the velocities of the points initially increase and then decrease. The second inflection point lies at the core, where the velocity is approximately zero in the beginning and then continuously increases until it reaches the velocity of the incident flow. The height of the wind gradient can be defined as the height when the velocity increases from zero to the velocity of the incident flow. From section 0 to section 4, the height of the gradient wind continues to increase. From section 4 to section 6, within the scope of the interaction between the conical vortices, the height of the gradient wind remains stable. However, from section 7 to section 10, the height starts to decline gradually. In summary, the height of gradient wind fluctuates in a parabolic manner on the roof surface. For visual plane 3, in section 6, where the vortex core lies, the velocities above the vortex core increase linearly to the velocity of the flow. Hence, the height of gradient wind exhibits a steady increase from section 0 to 10.

3.2 The trajectory of the vortex core in uniform flow (instantaneous characteristics)

Fig. 7 shows instantaneous streamlines of conical vortices at different moments in visual plane 2. As Fig. 7 illustrates, the conical vortices resize and sway constantly all the time, showing its intermittent characteristics. The conical vortex itself is smooth, only leads to stable suction, and will not cause fluctuation suction. Nevertheless, the fluctuations in suction are due to the

low-frequency sway of the conical vortices separated from the edges of the roof and the high-frequency rotation of the spiral axes of the conical counter-rotating vortices (Kawai and Nishimura 1996). In Fig. 7(a), the secondary vortex is clearly observed near the main vortex at the time of 0.045 s. The main and secondary vortices combined into an eddy in the next moment of 0.005 s. Due to a velocity component flow along the windward direction, the dissipation vorticity within the vortex occurs to ensure constant supplementation of the energy and balance of the vortex. After some interval of time, the reattachment of the separated shear layer from the main vortex stream near the surface creates a secondary vortex. Even there will be a new vortex called the third vortex is created. The tertiary vortex is therefore formed by the secondary vortex, as shown in Fig. 7(c). Fig. 8 depicts the results of the instantaneous position of the conical vortex in visual plane 2. The X coordinate in the figure refers to the horizontal distance of the vortex core from the windward edge (along the intersecting line of visual plane 2 and the roof), while the Z coordinate represents the vertical height of the vortex core from the roof. The cores of the vortices are mainly concentrated in the segment of 50 mm to 100 mm, and the core heights are very high in this section, in the range of 10 mm to 20 mm.

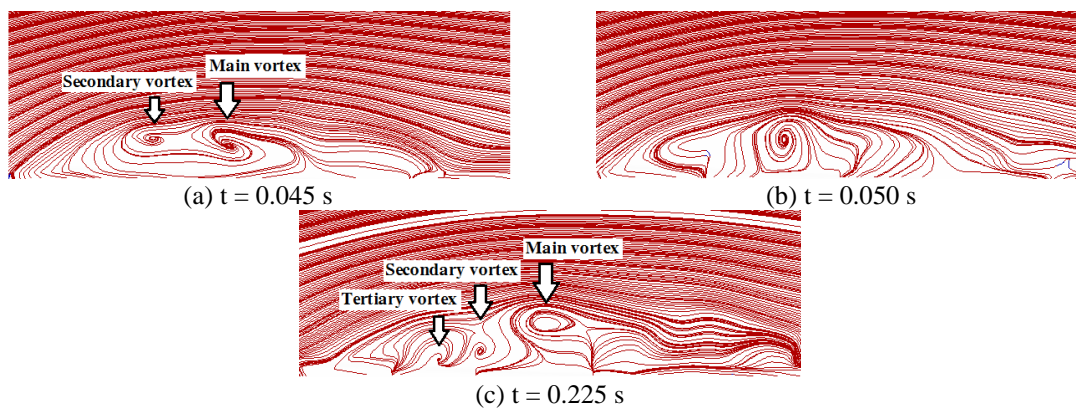


Fig. 7 Instantaneous characteristics of the conical vortices (uniform flow)

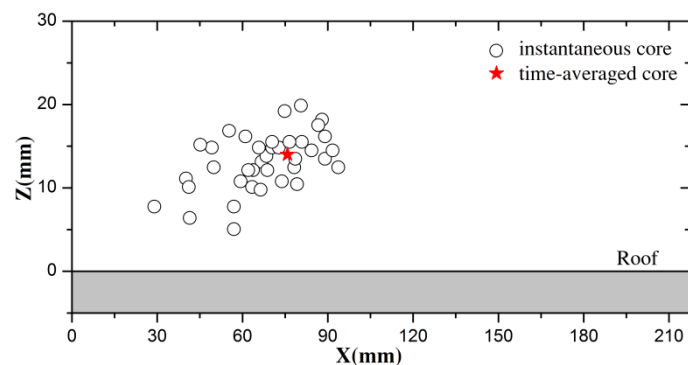


Fig. 8 Instantaneous position of the vortex core (uniform flow)

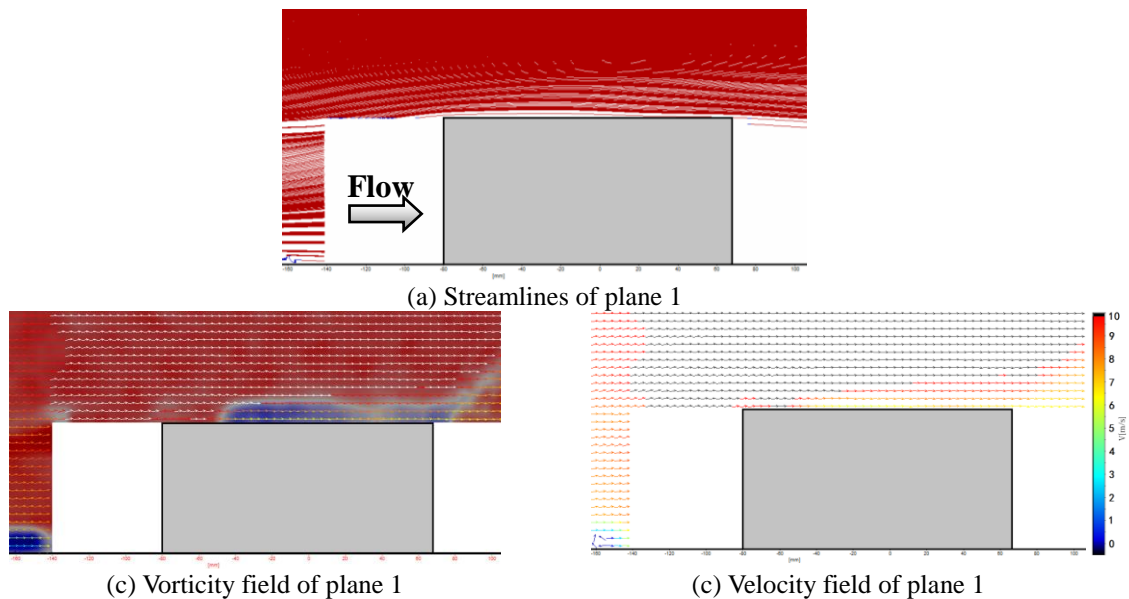


Fig. 9 Streamlines, vorticity and velocity vector field of the conical vortices (turbulent flow)

3.3 Conical vortices in turbulent flow (time-averaged characteristics)

The streamline and vorticity flow field in visual plane 1 at a wind direction of 15° are apparent in Fig. 9. Similarly, no eddy was observed to occur in the grid-generated turbulent flow, and the streamlines were slightly bent. However, the streamlines are much denser in the turbulent stream, mainly due to the increasing turbulence, which caused the mixing movement of the fluid particles to be more intense. The velocity of most regions over the roof is equal to the approaching flow, and the velocity close to the roof surface is approximately 0.7 times of the incoming flow. The negative vorticity was distributed over the central roof with a small absolute value. The vorticity far from the roof surface is approximately zero, which further proved that no eddy existed.

Figs. 10 show the streamline and vorticity distributions according to an ensemble average taken at plane 2 and plane 3 in grid-generated turbulent flow. These results are far different from those of uniform flow: the conical vortex section is flatter and the sphere of influence induced by vortex is greatly reduced compared to the uniform flow case. Note that the distance between the vortex core and the windward wall edge is decreasing with increasing turbulence intensity. In addition, the angle between conical vortex axis and the main leading edge also increased. The peak negative vorticity still appeared over the edge zone of the windward wall, where the separated shear layer meets the reverse flow to create a wedged region. The vorticity value reduces because the flow heads to the rear of the roof surface, which indicates that the conical vortex is continuously rolling around the vortex axis. A positive vorticity with a small value is well distributed between the vortex core and the roofs, indicating no obvious effect from the vortices. By contrasting the results of visual plane 2 with the results of plane 3, the vortex core heights are found to be at nearly the same level, and the distance of the vortex core from the main windward edge at visual plane 3 is slightly larger than that of plane 2.

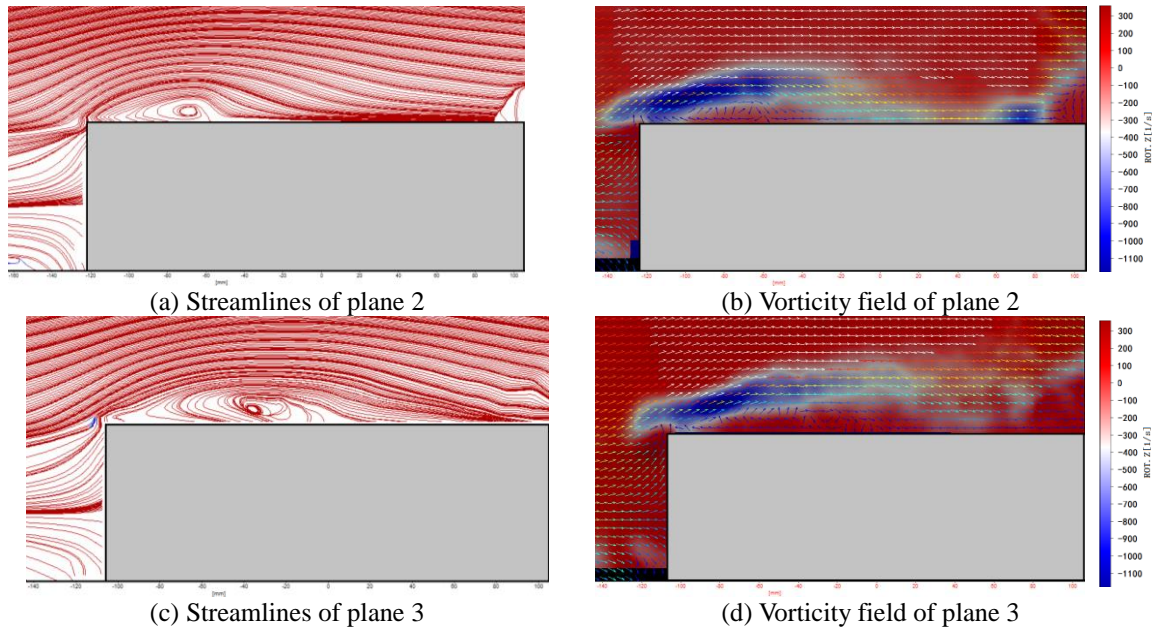


Fig. 10 Streamlines and vorticity field (turbulent flow)

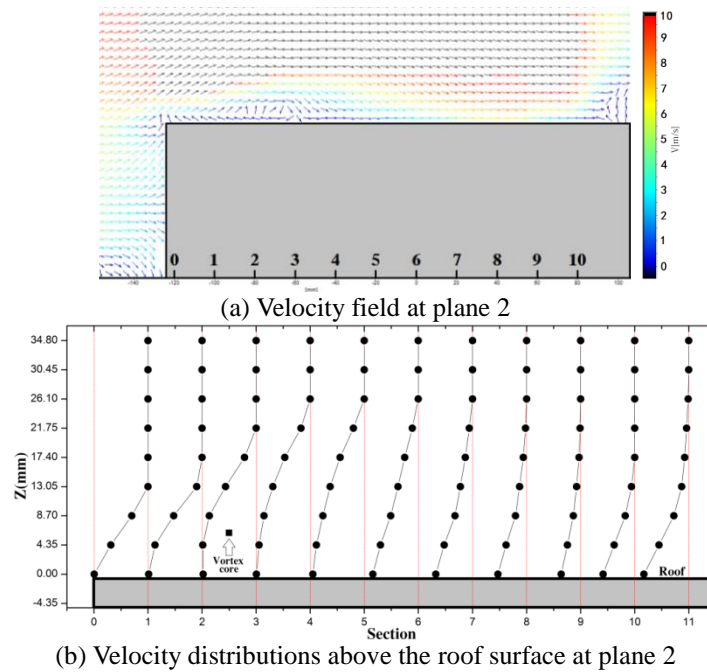


Fig. 11 The distribution of the along-wind direction velocity (turbulent flow)

The average velocity vector fields and velocity distributions above the roof surface captured on the different planes for plane 2 and plane 3 are shown in Figs. 11 and 12, respectively. Note that the velocity vector below the vortex core that clings to the roof surface remains near zero. However, the velocity of the region at the rear of the roof in visual plane 2 initially increased, and then decreased gradually as the flow headed downstream. In this study, the height of the vortex is 13.13 mm and the horizontal distance between the vortex core and the main windward edge is 70.37 mm in uniform flow, while for the turbulent stream with intensity of 10%, the height is 5.51 mm and the horizontal distance is 53.91 mm, i.e., only approximately half that in uniform flow. This result again verifies that, with the increase in turbulence intensity, the vortex core height and the distance away from the windward edge are both reduced. From section 0 to section 3, the gradient wind height increases in this range, with an obvious effect from the corner vortices. From section 4 to section 9, the gradient wind height is fairly stable. With the start of section 9, the gradient wind height exhibits a gradual trend of ascending first and then descending in succession, with the changes in the shape of a parabola. Relative to visual plane 3, the vortex core of the roof recirculation zone was found to be at section 3, and within the scope of sections 0 to 10, the gradient wind height exhibits a steady increasing trend.

3.4 The trajectory of the vortex core in turbulent flow (instantaneous characteristics)

One of the main conclusions from examining the vortex image, shown in Fig. 13, is that the vortex changes position and size rapidly and considerably in turbulent flow. The majority of this instantaneous motion is attributable to the unsteady flow field because it can produce a large pulse and cause more intense fluctuating wind pressure on the roofs.

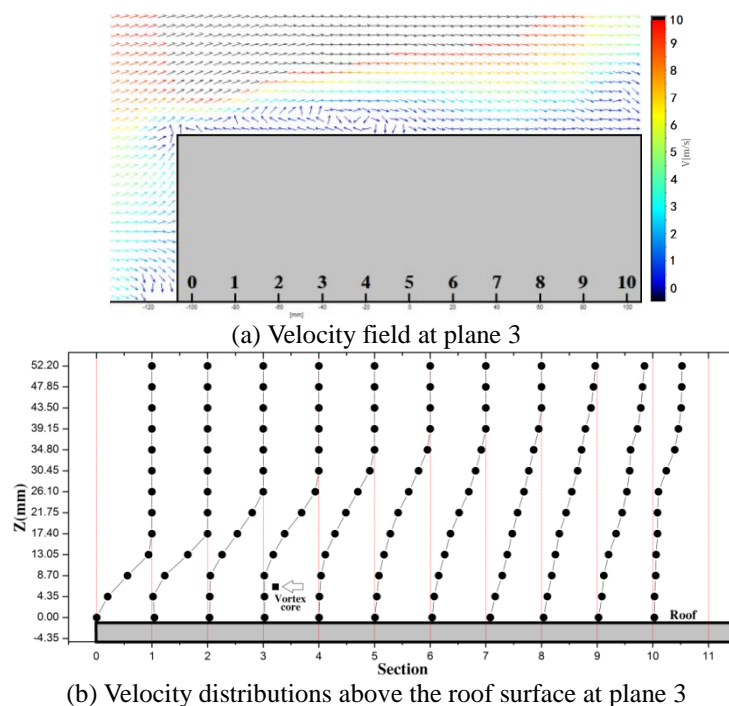


Fig. 12 The distribution of the along-wind direction velocity (turbulent flow)

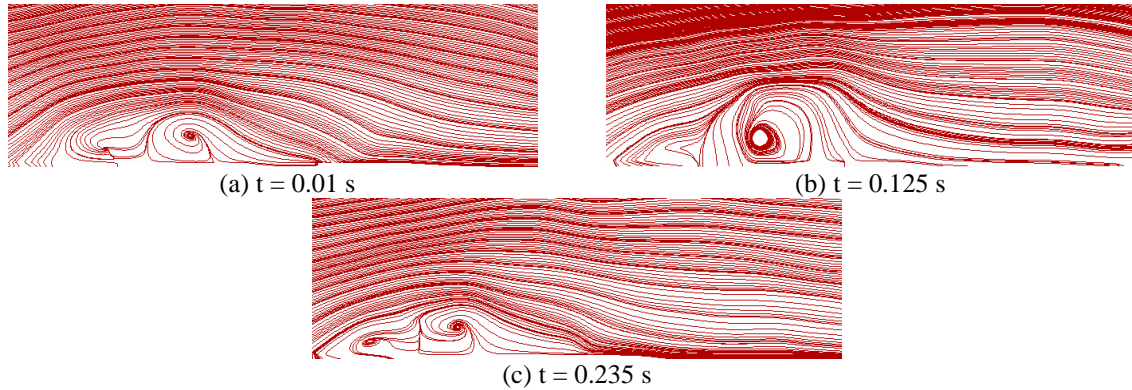


Fig. 13 Instantaneous characteristics of the conical vortices (turbulent flow)

The turbulence intensity is an important antecedent for the structure morphology for which the effects of various scales of turbulence components on conical vortices also vary. Small-scale velocity fluctuations are expected to influence entrainment and thus control the process whereby the upward flow is separated at the upwind roof edge and the downward flow forms the frontal eddy. Medium-scale velocity fluctuations are expected to accelerate the vortex spin without changing its position or size, and large-scale fluctuations will cause the vortex to move its position (Banks and Meroney 2001).

In a uniform flow field, due to the lack of different scale turbulence components in approaching flow, the low-frequency pulse composition is close to zero in the vertical wind spectrum, and the high-frequency composition is slightly greater, but not obvious, thus, the movement of the conical vortex is relatively moderate. On the contrary, all scales of turbulence components are observed in turbulent shear flows, with the small-scale components prompting the separated shear layer to be attached to the roof earlier. Hence, the conical vortex axis is closer to the leading edge, thereby causing a much smaller size of vortex in the turbulent flow field. The combination of turbulent vortex cores of instantaneous location images (Fig. 14) can be confirmed: with the increase in the turbulence intensity, the velocity changes drastically over time and distance; most of the instantaneous vortex core is focused in the first half of the area of the roof, and the vortex core height is lower.

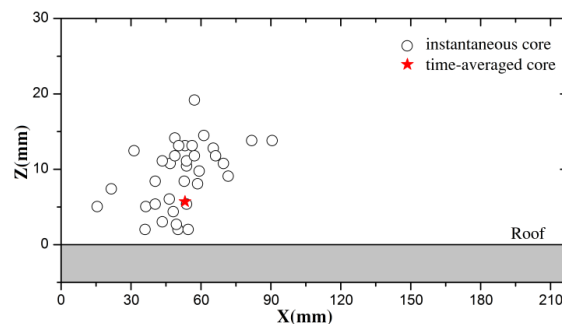


Fig. 14 Instantaneous position of the vortex core (turbulent flow)

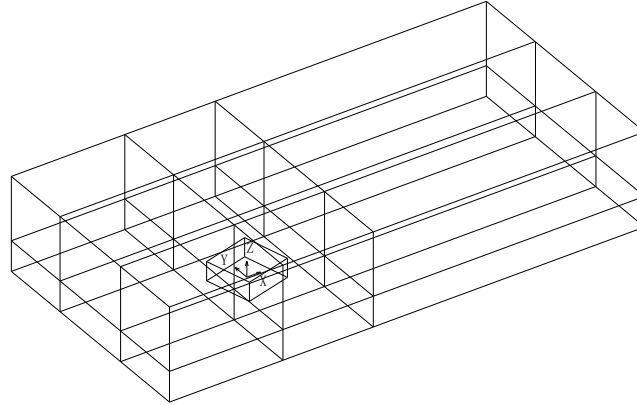


Fig. 15 Model and watershed area

4. Numerical simulations

4.1 Geometric modeling and mesh generation

For comparison with the flow visualization experiment results, the simulation model dimensions coincide with the experiment model dimension ($L \times W \times H = 0.21 \text{ m} \times 0.21 \text{ m} \times 0.084 \text{ m}$), and the watershed area has the dimensions of $4.2 \text{ m} \times 2.1 \text{ m} \times 0.42 \text{ m}$. The model was started at the third region in the flow direction, as shown in Fig. 15. The model was packaged with a larger cube outside, and the internal regions were simulated using an unstructured tetrahedral mesh, while between the larger cube and the watershed area, a hexagonal structured mesh was used. The mesh close to the cylinder was quite dense; in contrast, away from the cylinder, the interface area was sparse. Compared with the fully unstructured grids, calculations in this study suggest that the accuracy of the hybrid grid method is improved. After the processes of initialization and refinement, the whole hybrid grid basin partition comprised 1.38 million cells.

4.2 Turbulence model

The standard $k-\varepsilon$ model introduces the isotropy eddy viscosity hypothesis, for which C_μ is regarded as a constant. Many of the new models are proposed to overcome the defects, such as the realizable $k-\varepsilon$ model. The primary improvement of the simulation model is made in the values of C_μ and the dissipation rate control equation. C_μ was obtained using Eq. (1) (Tutar and Oguz, 2012).

$$C_\mu = \frac{1}{A_0 + A_s U^* \frac{k}{\varepsilon}} \quad (1)$$

Where $A_0 = 4.0$, $A_s = \sqrt{6} \cos \phi$, $\phi = \frac{1}{3} \cos^{-1}(\sqrt{6}W)$, $W = \frac{E_{ij}E_{jk}E_{kj}}{(E_{ij}E_{ij})^{1/2}}$, $E_{ij} = \frac{1}{2} \left(\frac{\partial u_i}{\partial x_j} + \frac{\partial u_j}{\partial x_i} \right)$

$$U^* = \sqrt{E_{ij}E_{ij} + \tilde{\Omega}_{ij}\tilde{\Omega}_{ij}}, \quad \tilde{\Omega}_{ij} = \Omega_{ij} - 2\varepsilon_{ijk}\omega_k, \quad \Omega_{ij} = \bar{\Omega}_{ij} - \varepsilon_{ijk}\omega_k$$

As seen above, C_μ is a function of the average stress and the rotation rate; additionally, the calculation precision in boundary layer was improved compared to the case of assigning a constant of 0.09. In addition, the dissipation rate equation can be expressed as

$$\frac{\partial(\rho\varepsilon)}{\partial t} + \frac{\partial(\rho\varepsilon u_i)}{\partial x_i} = \frac{\partial}{\partial x_j} \left[\left(\mu + \frac{\mu_t}{\sigma_\varepsilon} \right) \frac{\partial \varepsilon}{\partial x_j} \right] + \rho C_1 E \varepsilon - \rho C_2 \frac{\varepsilon^2}{k + \sqrt{\nu \varepsilon}} \quad (2)$$

where

$$\sigma_k = 1.0, \sigma_\varepsilon = 1.2, C_2 = 1.9, C_1 = \max \left(0.43, \frac{\eta}{\eta + 5} \right), \eta = (2E_{ij} \bullet E_{ij})^{1/2} \frac{k}{\varepsilon}$$

Compared with the Standard $k-\varepsilon$ model in the numerical simulation of the flow around a blunt body, the realizable $k-\varepsilon$ model has the following merits: 1. agreement with the real Reynolds stress turbulence; 2. simulation of the spread of the plane and the round jet speed can be more accurate; and 3. better performance of the separated flow and the secondary flow using the complex flow calculation. Therefore, the realizable $k-\varepsilon$ model was chosen in this paper.

4.3 Boundary conditions

The inlet zone type was set as the velocity-inlet for the define boundary conditions. The x axis indicated the entrance velocity direction, and the magnitude of the velocity was 10 m/s. The turbulence specification method was given by the intensity and the length scale. The outlet zone type was set as out-flow. The normal gradient of all flow variables in the flow field along the direction of outlet was zero. The flow variables on the border were determined using the extrapolation method and were found to have no effect on the upstream flow. The top, broadsides, and ground of the watershed area and the model surfaces are based on the no wall-slip assumption. The results obtained through using the non-balance wall function were close to the experimental measurements in the high Reynolds number flow, which takes into account the effects of the pressure gradient and deviates from the equilibrium assumption. Software simulation indicates that this method has high accuracy for complex flow calculations, such as the regions of surroundings, the separation, the reattachment and the collisions.

4.4 Simulation results

The geometric location of the conical vortices is shown in Fig. 16, where θ is the incident wind angle, α is the horizontal angle between the line of vortices centers and the windward edge, and β is the vertical angle between the line of vortices centers and the roof surface.

4.4.1 Comparison analysis of the vortex core position

Fig. 17 shows the streamline patterns in the cases of a 15° angle at visual plane 2 of the experiment and the corresponding simulation results. Table 1 presents the vortex core position at visual plane 2 and plane 3. The results show that the numerical simulation results and test results do not agree very well, particularly, in turbulent streams. The reasons for these differences are as follows: first, because of limited testing facilities, friction occurs around the wind tunnel wall. Therefore, the approaching flow was not a true smooth stream. Second, the PIV model with a certain radius at the edge of surfaces and the error has an effect on the shear layer separating from the leading edge. Third, to enhance the computing efficiency, the meshing that was close to model is quite dense; in contrast, away from the model, a fairly coarse (not too fine) mesh scale was used. Therefore, the uneven grid division influenced the precision of the calculations. Overall, the results from both the experiment and the numerical simulation coincide quite well, which demonstrated the validity of the simulation.

4.4.2 Surface pressure field at the visual plane

Figs. 18 and 19 present the results of the surface mean pressure coefficients ($C_{p_{mean}}$) and root-mean-square ($C_{p_{rms}}$) pressure coefficients measurements for the case $\theta = 15^\circ$ in uniform and turbulent streams. First, as expected in Fig. 18, for visual plane 1, it is clear that the peak mean and rms pressure are both near the leading edge. The effect of wind pressure decreases gradually with the increase in distance from the leading edge. At the same time, the indent flow has little effect on the rms pressure oscillation amplitude. Second, for visual plane 2, it appears that, compared to plane 1, the suction induced by conical vortices is more intense and the greatest suction exists in the middle region of the windward leading edge and the vortex core. This result occurs because the vertical angle between the streamline and the roof surface reached a maximum, which led to the worst upward entrainment suction on the roof. The peak rms pressure coefficient is distributed underneath the vortex core, indicating an obvious effect from the vortices. Third, visual plane 3 exhibits similar conditions as those of plane 2, for which a severe wind suction is still present at the leading edge and the rms pressure is more stable. The magnitude of the wind suction decreased with the flow developing downstream. Considering the results for the three visual planes, the associated strongest mean wind suction on the underlying surface is found to occur at visual plane 2, and the rms pressure coefficients were characterized by small fluctuations around a nearly constant value of approximately 0.1.

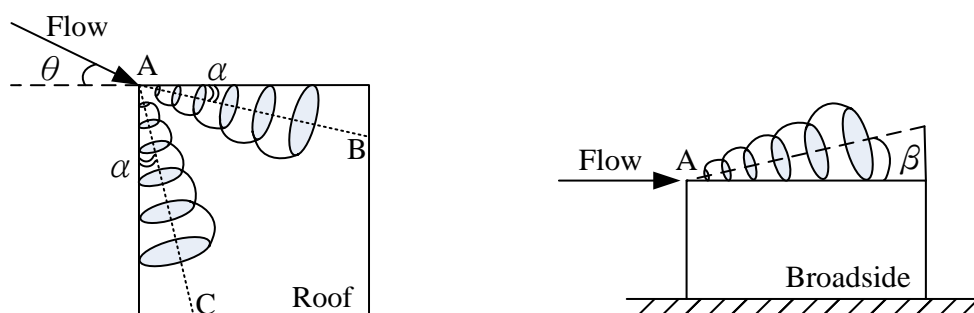


Fig. 16 Geometric locations of the conical vortices

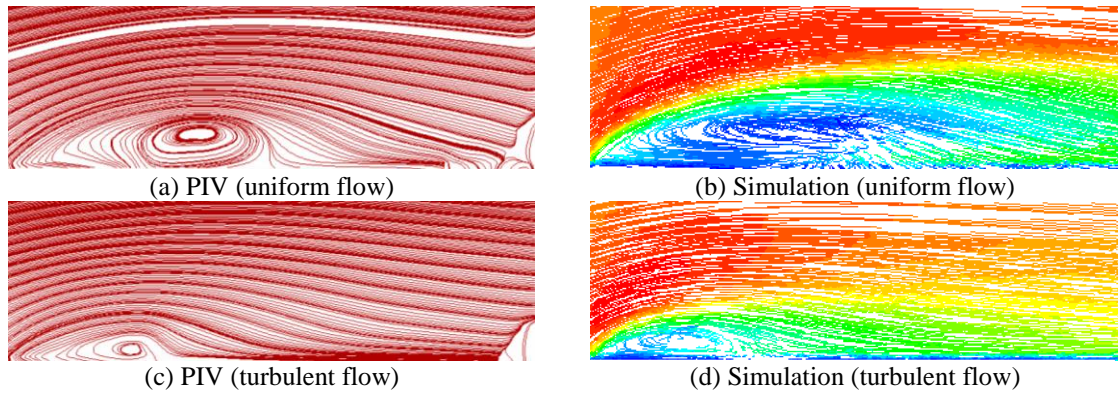


Fig. 17 Comparison of the experiment and simulation results (visual plane 2)

Table 1 vortex core position (unit: mm)

Flow	results	Visual plane 2				Visual plane 3			
		X*	Z [#]	α	β	X	Z	α	β
uniform	PIV	75.83	14.24	40°	7°	120.57	14.29	35°	4°
	Fluent	70.18	12.32	38°	7°	119.67	13.87	35°	4°
turbulent	PIV	51.91	5.51	32°	3°	71.59	6.67	24°	3°
	Fluent	48.03	5.05	31°	3°	70.37	6.05	24°	3°

*X: Vortex core's horizontal distance from the main windward edge; [#]Z: Vortex core's vertical height from the roof surface

As shown in Fig. 19, the general characteristics of the wind pressure curves in uniform and turbulent streams exhibit the same varying trend. However, in contrast to the grid-generated turbulent flow situation, the mean wind pressure is slightly larger, with a lower rms wind pressure, in uniform flow. This difference occurs because the upstream incoming wind acting on the roof surface directly results in the strong wind suction without meeting any obstacles. Due to the reduced variation of the scales of turbulence component in the incident flow, the rms pressure coefficient is smaller. The grid-generated turbulence field helped to increase the turbulence component due to the grid device, thereby increasing the fluctuating force; nevertheless, the kinetic energy of the incoming flow was being consumed by the grid device, thus directly resulting in the smaller suction. Therefore, the mean wind pressure induced by the conical vortices is larger and more destructive in uniform flow field, while the fluctuating pressure was significantly enhanced in turbulent streams.

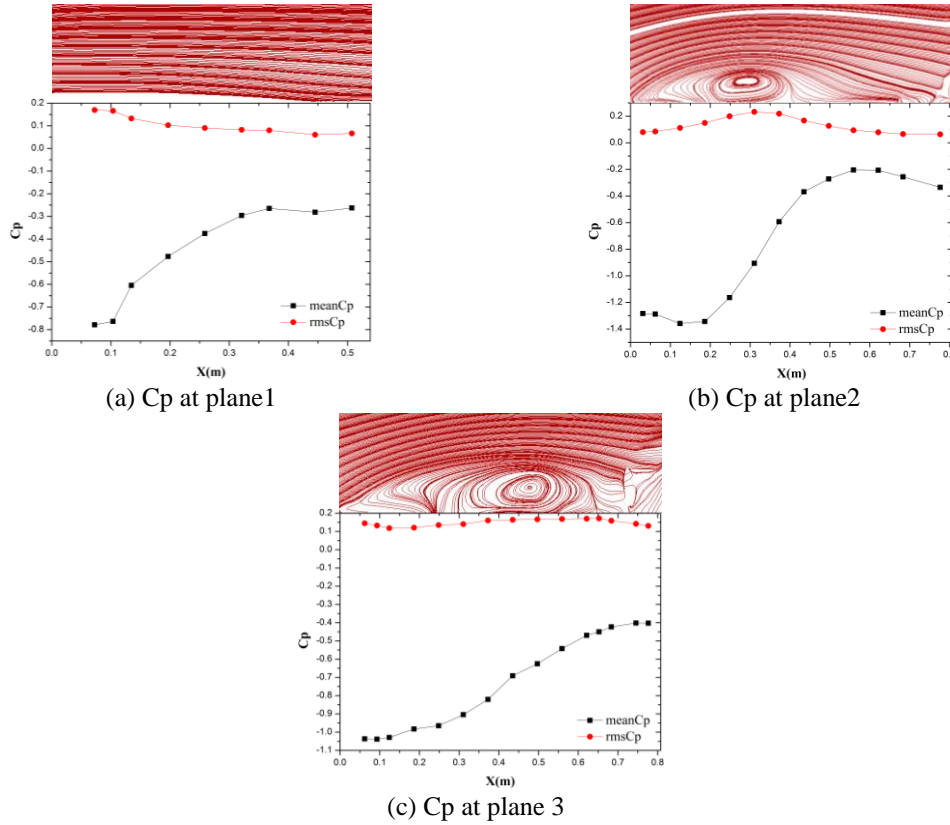


Fig. 18 Visual plane pressure under conical vortex (uniform flow)

4.4.3 Turbulent kinetic energy distribution

The turbulent kinetic energy (TKE) provides dynamic information regarding the corner vortices because it is caused by the swaying motion and turbulent fluctuating behavior of the vortices. TKE is also the measure of the turbulence growth or decay. Turbulent kinetic energy distributions can be defined by using Eq. (3).

$$q^2 = \frac{1}{2}(u^2 + v^2 + w^2) = \frac{3}{4}(u^2 + w^2) \tag{3}$$

Where u, v and w are the fluctuating velocity components in the wind direction, crosswind direction and vertical direction, respectively; $v^2 = \frac{u^2 + w^2}{2}$ is assumed because the crosswind velocity v cannot be measured on the x - z measurement plane. This assumption appears reasonable, based on wind tunnel data (Arie and Rouse 1956). In turbulence intensity profiles of a shear layer, the u, v and w three directional components have similar shapes in their distributions. The magnitude of the v component was also found to be somewhere between the magnitudes of u and w .

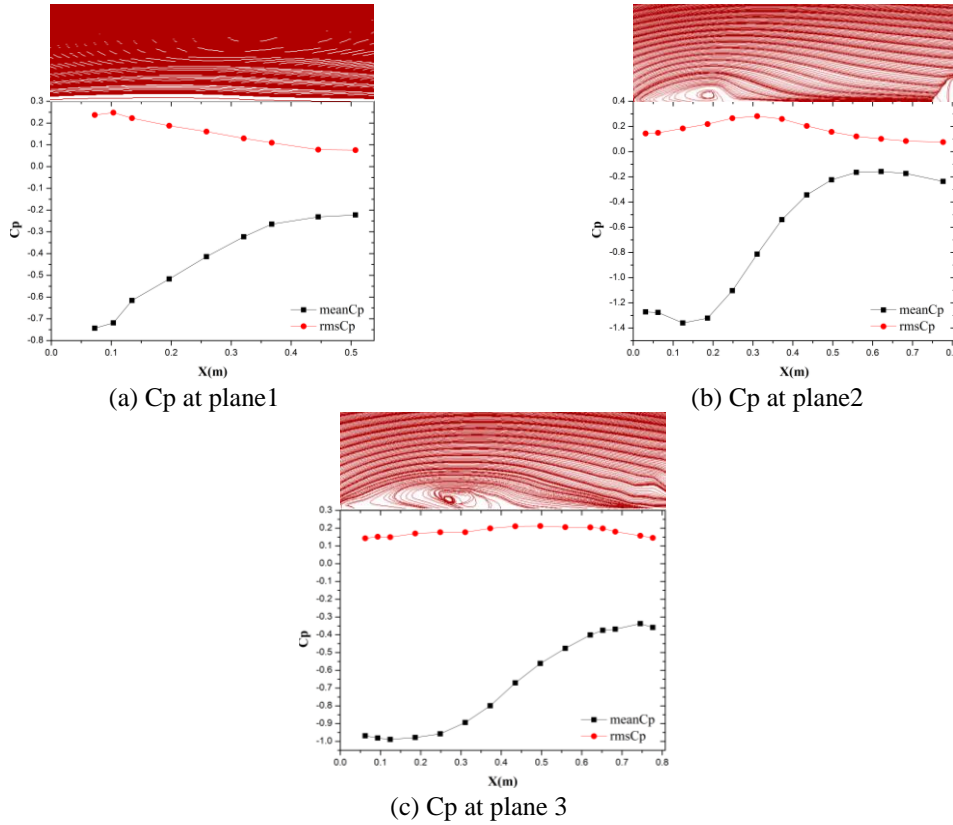


Fig. 19 Visual plane pressure under conical vortex (turbulent flow)

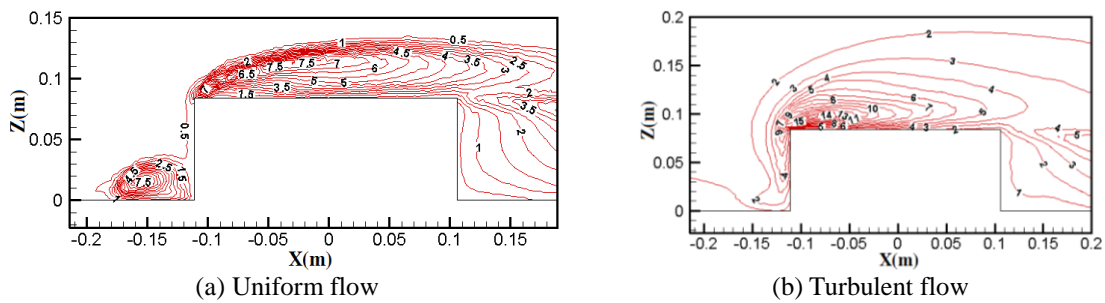


Fig. 20 Turbulent kinetic energy distribution

Fig. 20 represents the TKE distributions around the roof surface at visual plane 2 in uniform and turbulent streams. Most of the TKE appears to be concentrated on the recirculation zones on the roof surface, and the wake zone is at a relatively low level. For the uniform streams, the maximum TKE was found in the center of the horseshoe vortex in front of the windward wall. On the roof surface, the highest TKE was generated near the upper boundary of the roof recirculation zone, where the flow separated from the sharp roof edge accelerates and the separated layer has a

large velocity gradient. The location of the maximum TKE generated near the leading edge appears dispersed, and its intensity is spread as the flow goes downstream. However, the TKE in the turbulent flow field is significantly larger than the uniform stream, which is approximately two times higher. Once again, under the grid-generated turbulence, the movement of the conical vortex on the roof surface is proven to be more intense, and the fluctuating pressure is found to be significantly enhanced in turbulent streams.

5. 3-D characteristics of the conical vortices

Based on the results of fluent numerical simulations, clear views of the 3-D characteristics of the conical vortices and the wind pressure distribution on the vortex structures were obtained by combining the data of five equally spaced sections, which are perpendicular to the diagonal on the roof. The following conclusions can be drawn from Fig. 21:

- In the uniform flow field, when wind approaches a building oblique to one of its walls, the obstructed flow is forced to go over the building and the up-wash flow separates at the leading apex. The attack angle of the wind is not perfectly symmetric relative to the roof (15°) and is almost parallel to the secondary windward edge. Reduced flow wash-up over this side caused the lack of recognizable conical vortices. Generally speaking, the overall section of conical vortices is oblong and elongated, and the eddy clings to the roof surface, which is a certain distance away from the leading edge. The cross-sectional area grows as the flow heads downstream. The conical vortex is well developed at the location of the roof surface diagonal. From the last cross section, the conical vortex adhering to the roof is found to have moved out of the roof area, no longer being completely close to the roof, as in the windward area. Because attenuation of the vortex occurred gradually, the effect from the vortices strength decreases is obviously reduced. When studying the streamlines along the vertical wall, the horizontal momentum of the flow clearly started to transform into a vertical momentum further upstream on the windward wall. This behavior can explain why the windward pressure coefficients express positive values. On the contrary, weaker suction is induced by vortices at the secondary windward wall. A closer look at the roof surface pressure near the leading edge reveals that there exists a long and narrow region where the separated shear layer meets the reverse flow and the flow inside this area is highly turbulent and with a high gradient. As the flow developed downstream, the area of the conical vortices caused by the separated boundary layer increases with continuously reduced suction. This result is the key factor that exercises a great influence on the surface wind pressure characteristics.
- Similar trends were observed from the characteristics of the conical vortices and the wind pressure distribution on the roof in the grid-generated turbulent flow field. However, individual differences remain. On the one hand, the sectional area of the conical vortex in a turbulent stream is significantly less than in the uniform flow conditions, with a low vortex core height, and the distance from the leading edge of windward wall is also decreased; on the other hand, from the pressure distribution, the increase of turbulence is found to have a certain influence on the distribution of wind pressure. The mean pressure of the roof surface is more intense for the uniform stream, while the fluctuating wind suction becomes the outstanding problem for the turbulent stream, along with a larger intense suction area. Therefore, when designing engineering structures, the area of the windward edge requires special attention.

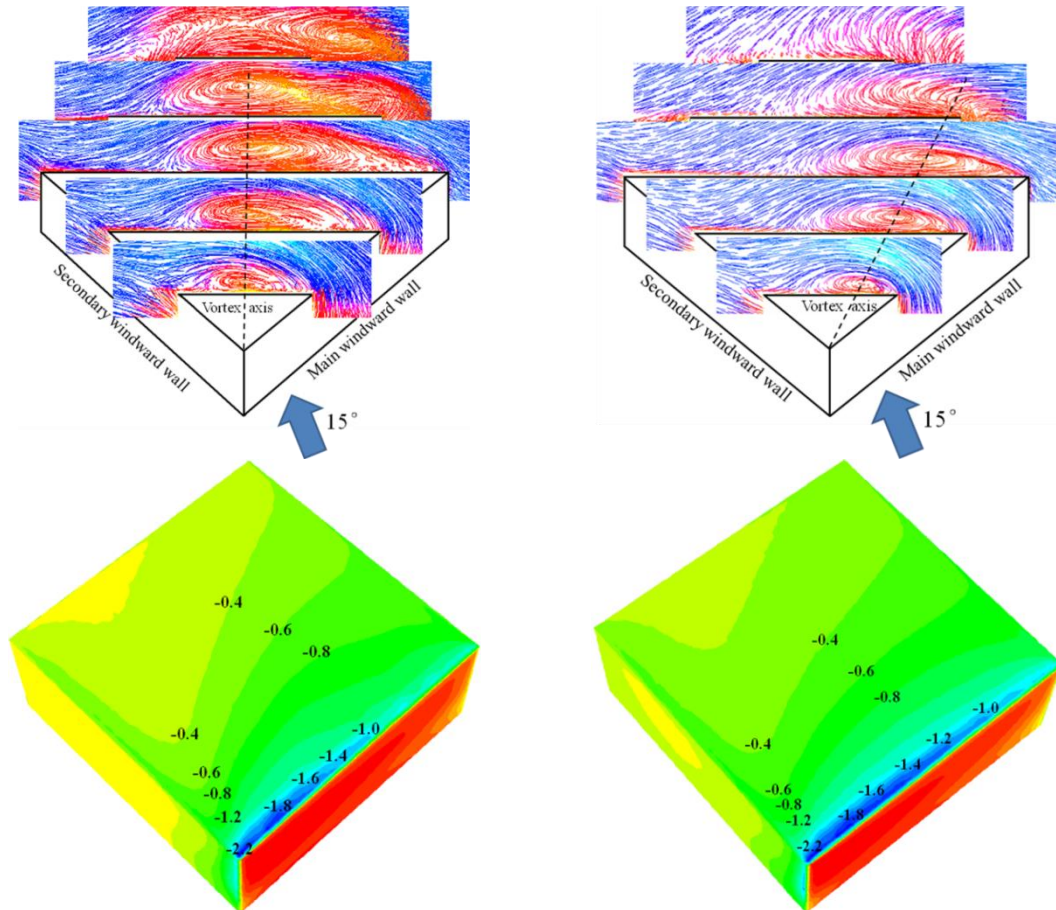


Fig. 21 3-D view and mean wind pressure coefficient distribution of the conical vortices

6. Conclusions

For the asymmetric flow with the attack angle of 15° , the conical vortices on a roof corner were investigated via PIV measurements. Clear views and rich information on the vortex structures were obtained by measuring the streamlines, the mean and instantaneous velocities, and the vorticity fields. Fluent was used to simultaneously validate the test results; these simulated values were found to be in agreement with the PIV results. Detailed 3-D flow structures and information on the wind pressure distribution were finally obtained. The main points discussed in this paper can be summarized as follows:

- Whether the approaching flow is uniform or is a turbulent stream, the shear layer may swirl around the roof surface for oblique wind. The vortex appeared at one side, for which the approaching flow direction was close to being parallel to the secondary windward side at the wind angle of 15° . The conical vortex has an oval shape, as seen in the cross-section for the two types of working conditions. The cross-sectional area of the conical vortex increases during the transition from when it appears to when it develops, and the vortex core height and the

cross-sectional area for the uniform stream are larger than for the turbulent stream, although the vortex axis position is closer to the windward edge for the turbulent flow field.

- Regardless of whether the approaching flow is uniform or turbulent, the increased turbulence intensity did not have an effect on the peak vorticity value because the vorticity and strain rate are determined by the velocity gradient of the flow field. Moreover, the mean pressure on the roof surfaces decreases, and a more drastic fluctuating suction increases are observed with the turbulence intensity. The maximum TKE occurred at the center of the roof recirculation zone and is generally reduced annularly outwards.
- Whether the approaching flow is uniform or turbulent, the mechanism of peak-pressure generation associated with the conical vortex is governed at the leading roof corner with a narrow area. A triangle shaped negative pressure zone appeared downstream. The mean pressure below the vortex core does not reach the peak, and the vorticity and wind suction are both reduced as the flow heads downstream.
- The conical vortex is subject to constant progress of motion and change due to the continuous pressure fluctuations. The vortices induced by the shear layer experience the processes of initial appearance, development, maturation, and vortex shedding. The vortex axis resizes and sways constantly, which reveals its intermittent characteristic. When the vortex breaks down in the end, a new vortex will be generated, and the process is repeated.

Acknowledgements

The essential contributions of the TJ-4 atmospheric boundary layer wind tunnel at the Wind Engineering Research Center of Tongji University are gratefully acknowledged. This work is supported by the National Outstanding Youth Science Fund Project (51125031) and Fundamental Research Funds for the Central Universities (3205005718), as well as the Colleges and Universities in Jiangsu Province Plans to Graduate Research and Innovation (KYLX_0157).

References

- Arie, M. and Rouse, H. (1956), "Experiments on two-dimensional flow over a normal wall", *J. Fluid Mech.*, **1**(2), 129-141.
- Banks, D., Meroney, R.N., Sarkar, P.P., Zhao, Z. and Wu, F. (2000), "Flow visualization of conical vortices on flat roofs with simultaneous surface pressure measurement", *J. Wind Eng. Ind. Aerod.*, **84**, 65-85.
- Banks, D. and Meroney, R.N. (2001), "A model of roof top surface pressures produced by conical vortices: Evaluation and implications", *Wind Struct.*, **4**(2), 1-20.
- Gu, Z.F., Yang, L.T. and Chen, Q.S. (2008), "Wind loading on plane roof of a large hangar", *Acta Scientiarum Naturalium Universitatis Pekinensis*, **44**(4), 501-506.
- Kawai, H. and Nishimura, G. (1996), "Characteristics of fluctuating suction and conical vortices in a flat roof in oblique flow", *J. Wind Eng. Ind. Aerod.*, **60**, 211-225.
- Kim, K.C., Ji, H.S. and Seong, S.H. (2001), "PIV measurement of roof corner vortices", *Wind Struct.*, **4**(5), 441-454.
- Li, J.G. (2007), "Flow-trace and Pressure Measuring Experiments of Boundary Layer Wind Tunnel and Standard Building Model", *Shanghai: Civil Engineering, Tongji University*.
- Tutar, M. and Oguz, G. (2002), "Large eddy simulation of wind flow around parallel buildings with varying configuration", *Fluid Dynam. Res.*, **9**, 289-315.

- Wu, F., Sarkar, P.P., Mehta, K.C. and Zhao, Z. (2001), "Influence of incident wind turbulence on pressure fluctuations near flat-roof corners", *J. Wind Eng. Ind. Aerod.*, **89**(5), 403-420.
- Ye, J.H. and Dong, X. (2014), "Improvement and validation of a flow model for conical vortices", *Wind Struct.*, **19**(2), 113-144.
- Zhao, Z. (1997), "Wind flow characteristics and their effects in low-rise buildings", *Lubbock, Texas: Civil Engineering, Texas Tech University*.

CC